



Research Paper

One-pot construction of 1D/2D $Zn_{1-x}Cd_xS/D-ZnS(en)_{0.5}$ composites with perfect heterojunctions and their superior visible-light-driven photocatalytic H_2 evolution



Wenhui Feng, Yaozhu Wang, Xueyan Huang, Kaiqiang Wang, Fan Gao, Yan Zhao,
Bo Wang, Lulu Zhang, Ping Liu*

State Key Laboratory of Photocatalysis on Energy and Environment, Fuzhou University, Fuzhou, 350002, PR China

ARTICLE INFO

Article history:

Received 12 May 2017

Received in revised form 2 July 2017

Accepted 1 August 2017

Available online 2 August 2017

Keywords:

$Zn_{1-x}Cd_xS$

$ZnS(en)_{0.5}$

Photocatalytic H_2 evolution

Heterojunction

Interfacial and interior carriers separation

ABSTRACT

A series of well-defined 1D/2D $Zn_{1-x}Cd_xS/D-ZnS(en)_{0.5}$ hybrids are fabricated via an one-pot synthesis method. The resulting composites exhibit enhanced visible-light-driven photoactivities for H_2 production from water in the presence of sacrificial reagents. The optimized $Zn_{0.41}Cd_{0.59}S/D-ZnS(en)_{0.5}$ hybrid shows the extremely high H_2 evolution rate of $463.6 \mu\text{mol H}^{-1}$ per 30 mg under visible light irradiation ($\lambda > 420 \text{ nm}$), without any cocatalysts. The highest H_2 production rate presents 826-fold and 24-fold enhancement compared to pristine $D-ZnS(en)_{0.5}$ and CdS , respectively. The corresponding apparent quantum yield (AQY) at 440 nm reaches up to 49.95%. The dramatically improved photocatalytic performance could be attributed to the effective interfacial and interior carriers separation. The former is based on the perfect $Zn_{0.41}Cd_{0.59}S/D-ZnS(en)_{0.5}$ heterojunctions with well-matched lattice and band structure, which is obtained by collaborative optimization of composition regulation and defect mediation. While the latter is achieved by low dimension control on the basis of the unique electronic behavior in low-dimensional materials. Besides, the stability of $Zn_{0.41}Cd_{0.59}S/D-ZnS(en)_{0.5}$ heterostructure is also investigated. Several possible causes of slight deactivation are proposed, which mainly includes the weakened interfacial contact, partial ethylenediamine (en) ligands dissociation or substitution by H_2O , OH^- and S^{2-} , repair of S vacancies and partial oxidation of Cd-S bonds. It may provide theoretic guidance for further designing high-stability photocatalysts. In addition, the optimized hybrid can be used at ambient pressure and under natural sunlight illumination, and the synthesis method is facile, economic and short-period. Thus our proposed system is highly attractive for large scale energy applications.

© 2017 Elsevier B.V. All rights reserved.

1. Introduction

Under the background of the worsening energy crisis and environmental issues, the exploitation and utilization of clean and renewable energy are of great urgency. Photocatalytic H_2 evolution is a promising way to convert the clean and inexhaustible solar power into chemical energy [1–8]. Naturally, photocatalytic splitting of water to produce H_2 has attracted extensive attention and become a topic of great interest in the world [9–14]. Unfortunately, the quantum efficiency of photocatalytic process is still too low to meet the global energy demand [15–17]. Hence, constructing high-efficiency photocatalyst system is an insurmountable challenge that we have been facing. To improve the photocatalytic efficiency,

various strategies have been developed during the past decades, such as textural and crystal modification, construction of interfacial heterostructure, non-metal or/and metal elements doping, noble metal loading, surface sensitization with different sensitizers (e.g. plasmonic nanostructures, polymers, dyes, semiconductors and surface-complexes), and coupling with other functional materials [18–21]. Among those strategies, semiconductor combination is one of the most common and promising methods for improving charge spatial separation efficiency [22]. As known, well-matched lattice and band structure of the combined semiconductors are two critical factors to construct an intimate and effective heterojunction [23,24]. However, on account of the limited alternative semiconductors with an appropriate intrinsic lattice and band structure, the semiconductor heterostructures usually suffer from serious lattice stress and poor band structure matching [24–27]. Thus, how to fabricate a perfect heterojunction for insuring efficient

* Corresponding author.

E-mail address: liuping@fzu.edu.cn (P. Liu).

transport pathway would be the key of developing high-efficiency heterostructures.

Alternatively, $Zn_{1-x}Cd_xS$ possesses continuously tunable lattice constant and bandgaps that could provide more opportunities for constructing effective heterojunctions via modulating the matching of lattice and band structure by changing the ratio of zinc to cadmium [28–31]. As a low-toxic and low-cost solid solution, $Zn_{1-x}Cd_xS$ has been proven to be a promising efficient visible-light-responsive photocatalyst recently [29,32–37]. Rapid recombination of photogenerated electron and hole during photocatalytic process, however, still restricts its wide application [36,38]. Benefiting from its flexible bandgap and band edges position, various $Zn_{1-x}Cd_xS$ -involved heterostructures with a soaring photoactivity by integrating $Zn_{1-x}Cd_xS$ with other materials have been developed [24,28,30,38–50]. Nevertheless, the intimate interfacial junction only facilitates the separation of the charge carriers distributed near the heterointerface. While a large proportion photoinduced carriers would be inevitably recombined during the migration from interior to surface in each semiconductor [38], that would lead to limited enhancement of photoactivity. Thus, systematically fabricating heterostructures, considering optimization of both internal and interfacial carriers separation to maximize the efficiency of charge utilization, would be a potential strategy for further improving the photocatalytic efficiency of heterostructure system. It is also an important step for the commercialization of $Zn_{1-x}Cd_xS$ -based photocatalysts.

Recent years have witnessed the increasing attention in low-dimensional materials for their unique electronic behavior in different confined dimensions [51–61]. Among them, one-dimensional (1D) nanostructures could not only transfer quickly charge carriers along their axis, but also provide a short diffusion length perpendicular to the their axis [59,62–65]. Those would result in a low carrier recombination in the bulk of 1D nanostructure. On the other hand, two-dimensional (2D) materials possess excellent optical and electronic properties, while 2D layered nanostructures, with large surface areas, could also be good catalyst supports [66,67]. Furthermore, some 1D/2D hierarchical nanostructures have been demonstrated to show rapid carrier transfer along the axial direction and relatively large surface areas by integrating the respective advantages [68–71]. Besides, 1D $Zn_{1-x}Cd_xS$ nanostructure indeed exhibits a preferable photocatalytic activity in some previous study [39,45,63,72]. In the light of the above-mentioned consideration, it is expected that the integration of 1D $Zn_{1-x}Cd_xS$ and a proper 2D material, with less lattice stress and well-matched band structure, would facilitate effectively both surface and bulk carriers separation, yielding a boosting performance. However, it's still a challenge to achieve tunable band gaps and lattice structure by altering the composition, simultaneously maintaining well-defined 1D/2D multidimensional growth and band alignment for the target heterostructure [45]. Coincidentally, our recent work has demonstrated that layered defect-rich $ZnS(en)_{0.5}$ nanosheets ($D-ZnS(en)_{0.5}$ NSs) possesses numerous mid-gap defect states, which not only can induce defect states excitation and broaden the light absorption spectrum of $ZnS(en)_{0.5}$, but also may mediate the formation of the staggered energy band alignment (*i. e.* type II heterojunction) from straddling energy band alignment (*i. e.* type I heterojunction) of $Zn_{1-x}Cd_xS/D-ZnS(en)_{0.5}$ [73]. What's more, the well-matched coordination mode between ZnS slices in $ZnS(en)_{0.5}$ and $Zn_{1-x}Cd_xS$ respectively could provide an important guarantee for a perfect interface between $Zn_{1-x}Cd_xS$ and $D-ZnS(en)_{0.5}$. Thus, the integration of 1D $Zn_{1-x}Cd_xS$ and 2D $D-ZnS(en)_{0.5}$ should be a promising heterostructure model with well-matched lattice and band structure, exhibiting a superior photocatalytic performance.

Herein, we report a one-pot solvothermal synthesis of well-defined 1D/2D $Zn_{1-x}Cd_xS/D-ZnS(en)_{0.5}$ heterostructure. This

approach is more facile than the traditional methods (usually suffering multi-step procedure or a long time hydrothermal process) for fabricating $Zn_{1-x}Cd_xS$ -involved heterostructures [28,43,45,74]. In this reaction system, en not only acts as a starting material, but also serves as solvent and template to control nanocrystal growth. $Zn_{1-x}Cd_xS$ nanorods (NRs) with variable bandgaps (ranging from 2.45 to 3.00 eV) is achieved by changing the ratio of Cd/Zn. Due to the similar coordination mode for ZnS slices in both $ZnS(en)_{0.5}$ and $Zn_{1-x}Cd_xS$, heterojunctions with well-matched lattice structure would be formed. In general, the perfect heterostructure is obtained via collaborative optimization of dimension control, composition regulation and defect introduction. Owing to both effective interfacial and interior carriers separation, the optimal $Zn_{0.41}Cd_{0.59}S/D-ZnS(en)_{0.5}$ heterostructure exhibits very high hydrogen production rate (463.6 $\mu\text{mol H}^{-1}$ per 30 mg) under visible light irradiation ($\lambda > 420 \text{ nm}$), even without any cocatalysts. This superior H_2 evolution rate is about 826 and 24 times higher than that of pristine $D-ZnS(en)_{0.5}$ and CdS , respectively. Besides, the apparent quantum yield (AQY) at 440 nm reaches up to 49.95%. These results suggest that the co-optimization of the interior and interfacial carriers separation efficiency for heterostructure is a promising way to develop high-efficiency photocatalysts. Also, an optimized model is proposed for designing more perfect heterostructure photocatalysts. More practically speaking, the synthesis method is facile, economic and short-period, thus it is highly attractive for large scale energy applications.

2. Experimental

2.1. Materials

Zinc acetate dihydrate ($Zn(CH_3COO)_2 \cdot 2H_2O$), Cadmium acetate dihydrate ($Cd(CH_3COO)_2 \cdot 2H_2O$), Thiourea (CH_4N_2S) and ethylenediamine ($H_2NCH_2CH_2NH_2$) were purchased from Sinopharm Chemical Reagent Co. Ltd. (Shanghai, China). All materials were analytical grade and used without any purification process. Deionized (DI) water used in the synthesis came from local sources.

2.2. Synthesis of $D-ZnS(en)_{0.5}$ NSs and CdS NRs

$D-ZnS(en)_{0.5}$ NSs were synthesized by a solvothermal procedure. Typically, 2 mmol Zinc acetate dihydrate and 6 mmol Thiourea were dispersed into 20 mL DI water. Subsequently, the obtained solution was poured into 60 mL ethylenediamine under the ceaseless stirring until formation of an homogenous mixture. Then the mixed aqueous solution was transferred to a 100 mL Teflon-lined stainless steel autoclave and placed inside a preheated oven at 160 °C and the reaction was continued for 4 h. After the reaction system cooled down to room temperature naturally, the resulting precipitate was separated by centrifugation, washed with DI water and absolute ethanol for several times. Then the products were dried at 60 °C overnight in vacuum oven. CdS NRs were prepared via a similar procedure. Except that 2 mmol $Cd(CH_3COO)_2 \cdot 2H_2O$ used as cationic precursor.

2.3. Synthesis of $Zn_{1-x}Cd_xS/D-ZnS(en)_{0.5}$ composites

A series of $Zn_{1-x}Cd_xS/D-ZnS(en)_{0.5}$ hybrids were prepared by an facile solvothermal method. Firstly, $2u$ mmol $Cd(CH_3COO)_2 \cdot 2H_2O$, $2(1-u)$ mmol $Zn(CH_3COO)_2 \cdot 2H_2O$ (where u corresponds to the molar ratio of $Cd/(Cd + Zn)$ precursor, $0 < u < 1$) and 6 mmol Thiourea were dispersed into 20 mL DI water. Subsequently, the obtained solution was poured into 60 mL ethylenediamine under stirring until formation of an homogenous mixture. Then the resulting aqueous solution was transferred to a 100 mL Teflon-lined stainless steel autoclave and placed inside a preheated oven at 160 °C

and the reaction was continued for 4 h. After the reaction system cooled down to room temperature naturally, the resulting precipitate was separated by centrifugation, washed with DI water and absolute ethanol for several times.

2.4. Characterization

The crystal structures of the as-prepared samples were identified by X-ray diffraction using X-ray powder diffraction (XRD) patterns were carried out on a Bruker D8 ADVANCE X-ray diffractometer, with Cu K α radiation ($\lambda=0.15418\text{ nm}$), which operated at 40 kV and 40 mA. The scan rate was 0.5 ($2\theta\text{ s}^{-1}$). Scanning electron microscopy (SEM) images were obtained using a HITACHI SU8000 field-emission scanning electron microscope. Transmission electron micrographs (TEM), High-resolution transmission electron micrographs (HRTEM), high-angle annular dark field-scanning transmission electron microscope (HAADF-STEM) images and energy dispersive X-ray (EDX)-STEM elemental mapping were collected with a TecnaiG2F20 S-TWIN with an accelerating voltage of 200 kV. Samples for TEM analysis were prepared by dispersing the powder in ethanol under sonication firstly, and then dropping one drop of the suspension on a copper TEM grid coated with carbon films. UV-vis diffuse reflectance spectroscopy (DRS) was measured by a Carry 500 UV-vis spectrophotometer, in which BaSO₄ was served as the background. X-ray photoelectron spectroscopy (XPS) investigation was recorded on a Thermo Scientific ESCA Lab 250 system, with a monochromatic Al K α as the X-ray source, hemispherical analyzer, and sample stage with multi-axial adjustability to obtain the composition on the surface of samples. The N₂ adsorption/desorption isotherms were obtained on a Micrometrics ASAP 2020 analyzer at 77 K after the as-prepared samples were degassed at 110 °C for 300 min in a vacuum. Photocurrents were recorded on an electrochemical workstation (CHI 660E Instruments) with a conventional three-electrode system. The counter and reference electrodes were Pt plate and Ag/AgCl electrode, respectively, and electrolyte was Na₂SO₄ (0.2 M) aqueous solution. Electrochemical impedance spectroscopy (EIS) were measured using a ZENNIUM electrochemical workstation (Zahner, Germany), with the above mentioned three-electrode system and 0.35 M Na₂S and 0.25 Na₂SO₃ solution as electrolyte. 10 mg of the test sample was dispersed in 0.5 mL N,N-dimethyl formamide (DMF) solution by sonication, and 20 μL as-obtained slurry was then evenly spread onto a fluorine-doped tin oxide (FTO) conductor glass substrate with an area of 5 mm × 5 mm. After the samples covered on the glasses were dried, the parts without samples were painted by insulating epoxy resin. The obtained FTO glass were used as a working electrode. A 300 W xenon lamp equipped with a cut-off filter ($\lambda>420\text{ nm}$) was served as a light source for provide a visible light irradiation. Thermogravimetric analysis (TGA) was carried out with a TA SDT-Q600 analyzer. The TGA curves were recorded in the temperature range of 25 ~ 700 °C, at a heating rate of 10 °C min⁻¹ in N₂ surrounding.

2.5. Photocatalytic activity measurement

Typically, 30 mg as-prepared samples were dispersed into 100 mL solution containing 0.35 M Na₂S and 0.25 M Na₂SO₃, those act as the sacrificial reagents. The suspension was poured into a quartz flask, and vacuumed with a vacuum pump for 1 h to drive away the residual air. The photocatalytic water splitting to produce H₂ was carried out by vertically irradiating the suspension with a 300 W xenon lamp coupled with a cut-off filter ($\lambda>420\text{ nm}$). The temperature of reaction solution was keep at 5 °C. The gas product composition was analyzed every 1 h by an Techcomp 7900 chromatograph (GC) with TCD detector and Ar as the carrier gas. Apparent quantum yield (AQY) were measured by using a

440 ± 15 nm band-pass filter and calculated according to the following equation:

$$\text{AQY}(\%) = \frac{\text{number of produced H}_2\text{ molecules} \times 2}{\text{number of incident photons}} \times 100 \quad (2)$$

3. Results and discussion

Fig. 1A and B show the XRD patterns of the pure CdS (labeled as C), D-ZnS(en)_{0.5} (labeled as Z) and a series of Zn_{1-x}Cd_xS/D-ZnS(en)_{0.5} heterostructures. All hybrids are abbreviated as C-Z-*u*, where *u* corresponds to the molar ratio of Cd/(Cd + Zn) in each composite. The XRD pattern of CdS could be indexed as the hexagonal structure (JCPDS no. 89–2944) with good crystallinity. The three diffraction peaks at 24.8°, 26.5°, and 28.2° could be assigned to the (100), (002), and (101) planes, respectively. The XRD pattern of D-ZnS(en)_{0.5} is in agreement with that reported in our previous work. It reveals that D-ZnS(en)_{0.5} is a layered complex with orthorhombic structure [73]. For C-Z-*u* samples, on one hand, as the amount of Cd precursor increases, the diffraction peaks corresponding to (100), (002), and (101) planes gradually appear and the intensity of those peaks enhances, and the peak positions continuously shift to low-angle side. On the other hand, the intensity of the characteristic diffraction peaks assigned to D-ZnS(en)_{0.5} gradually decreases, and the location of the peaks are nearly unchanged. These results demonstrate that Zn_{1-x}Cd_xS solid solution gradually forms and increases, while the content of D-ZnS(en)_{0.5} in composite decreases constantly, as the Cd precursor increases. As reported, the lattice parameter of c of Zn_{1-x}Cd_xS solid solutions varies linearly with composition based on the Vegard's law [45,47]. We further estimate the *x* value of Zn_{1-x}Cd_xS in different samples, according to the lattice constant *c*, which is calculated from their diffraction peaks. The estimated results are listed in **Fig. 1C**.

To investigate the optical properties of the as-synthesized samples, the UV-vis diffuse reflectance spectra (DRS) displayed in **Fig. 2A** is analyzed. The pure Z sample exhibits an intrinsic absorption in the UV region and a weak wide visible light absorption originating from the rich defects [73]. While the pristine C sample has a broad absorption in the visible region. In the case of C-Z-*u* samples, all hybrids inherit a combination of the band edge absorption of Zn_{1-x}Cd_xS and the band edge and interband absorption of D-ZnS(en)_{0.5}. It further indicates that a series of composites containing Zn_{1-x}Cd_xS and D-ZnS(en)_{0.5} are synthesized successfully. It is also clear that there is an obvious and continuous redshift of the absorption edges for all composites with increasing *u*. The corresponding Eg values of all samples estimated by the Kubelka-Munk method are presented in **Fig. 2B**. It implies that the band gaps of the Zn_{1-x}Cd_xS solid solution in C-Z-*u* samples can be controlled in a wide range (from 2.45 to 3.00 eV) via the facile solvothermal process. In our case, the variation of the Eg of Zn_{1-x}Cd_xS with *u* value can be fitted with a function of Eg = 2.439 – 0.119 × ln(*u* – 0.011) (0 < *u* ≤ 1). In addition, the color of the samples changes gradually from white to orange with increasing the Cd content in final products as pictured in **Fig. 2C**. This phenomenon also agrees with the DRS results.

In order to reveal the microscopic architectures of as-prepared samples, Scanning electron microscopy (SEM) is employed. As shown in **Fig. 3A**, the pristine CdS sample appears to be nanorod morphology. In contrast, the pure D-ZnS(en)_{0.5} exhibits plate-like shape with non-uniform widths and lengths, whose thickness is about 40 nm as our previous reported (**Fig. 3B**) [73]. As for the C-Z-0.24 composite, the product shows a mixture of the nanorods and plate-like morphologies, with the nanorods (NRs) attaching on the nanosheets (NSs) evenly as shown in **Fig. 4C**. For further determining if the NRs belong to Zn_{1-x}Cd_xS and NSs correspond to D-ZnS(en)_{0.5} in the C-Z-0.24 hybrid, high-angle annular dark-

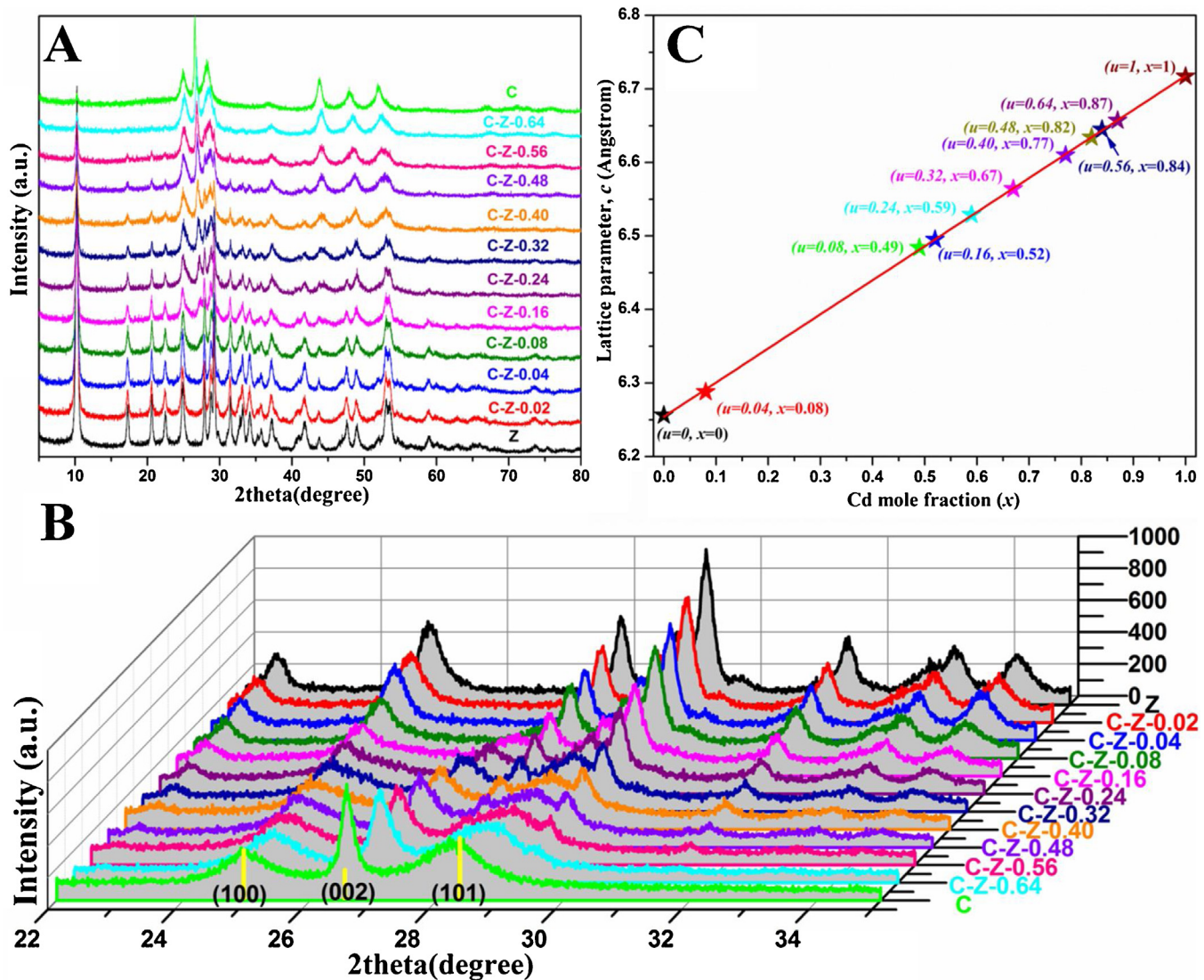


Fig. 1. XRD patterns of Z, C and C-Z-*u* samples (A and B). A linear relationship of the lattice parameters *c* (Å) as a function of Cd content (*x*) in $Zn_{1-x}Cd_xS$ composite (C).

field scanning transmission electron microscopy (HAADF-STEM) and energy dispersive X-ray (EDX)-STEM are carried out. As shown in Fig. 4A, 1D NRs and 2D NSs present different contrasts in C-Z-0.24 hybrid. It indicates that two of them have different chemical components. Furthermore, the elemental mapping images, collected from the area of yellow rectangular frame in Fig. 4A (enlarged image shown in Fig. 4B), are displayed in Fig. 4C-G. As displayed, C, N, S and Zn distribute homogeneously in the plate-like area, while S, Zn and Cd distribute homogeneously in the rod-like area. Meanwhile, notably, Cd only appears in the rod-like region, while Zn and S are concentrated more on overlap regions of NRs and NSs. These results confirm that $Zn_{1-x}Cd_xS$ and D-ZnS(en)_{0.5} exhibits rod-like and plate-like morphology, respectively. Besides, transmission electron microscopy (TEM) and high-resolution transmission electron microscopy (HRTEM) are also employed to reveal detailed structure of as-obtained C-Z-0.24 composite and confirm perfect heterojunctions existing in the $Zn_{1-x}Cd_xS$ /D-ZnS(en)_{0.5}. The TEM image in Fig. 5A also demonstrates that 1D NRs uniformly adheres to 2D NSs in C-Z-0.24 sample. The enlarged TEM image corresponding to the region in red rectangular box is shown in Fig. 5B. Further, the HRTEM images zooming in the particular area I and II are displayed in Fig. 5C and D, respectively. As exhibited, two mutually orthogonal sets of crystal lattice fringes, with the lattice

spacing of 0.340 nm and 0.311 nm in the NRs, are well matched with the (100) and (002) plane of hexagonal $Zn_{1-x}Cd_xS$, respectively. It further proves that 1D highly crystalline $Zn_{1-x}Cd_xS$ NRs are formed and the growth direction is mainly along the [002] direction. Meanwhile, various lattice fringes with different orientations in D-ZnS(en)_{0.5} NSs reveals the poly crystalline characteristics of D-ZnS(en)_{0.5}. Besides, it must be noted that several couples of criss-cross lattice fringes with very approximate lattice spacing values exist at the interface of $Zn_{1-x}Cd_xS$ /D-ZnS(en)_{0.5}. This result corroborates the conjecture that many perfect heterojunctions indeed be constructed successfully in C-Z-0.24 hybrid.

The photocatalytic performance of the as-prepared products with predicted structure is investigated through the evaluation of photocatalytic H₂ production by splitting water under visible-light irradiation ($\lambda > 420$ nm). In this photocatalytic reaction system, any noble metal as cocatalyst is absence, and 0.35 M Na₂S and 0.25 M Na₂SO₃ are used as hole scavengers. As presented in Fig. 6A, the pure D-ZnS(en)_{0.5} shows a limited visible light H₂ evolution rate (0.56 $\mu\text{mol H}^{-1}$ per 30 mg). As elevating *u* value from 0.02 to 0.24 for C-Z-*u* composites, the photocatalytic H₂ evolution rate increases dramatically, and subsequently reduces with further increasing Cd content. The highest H₂ production rate is up to 463.6 $\mu\text{mol H}^{-1}$ per 30 mg, which is approximately 826 and 24 times higher than

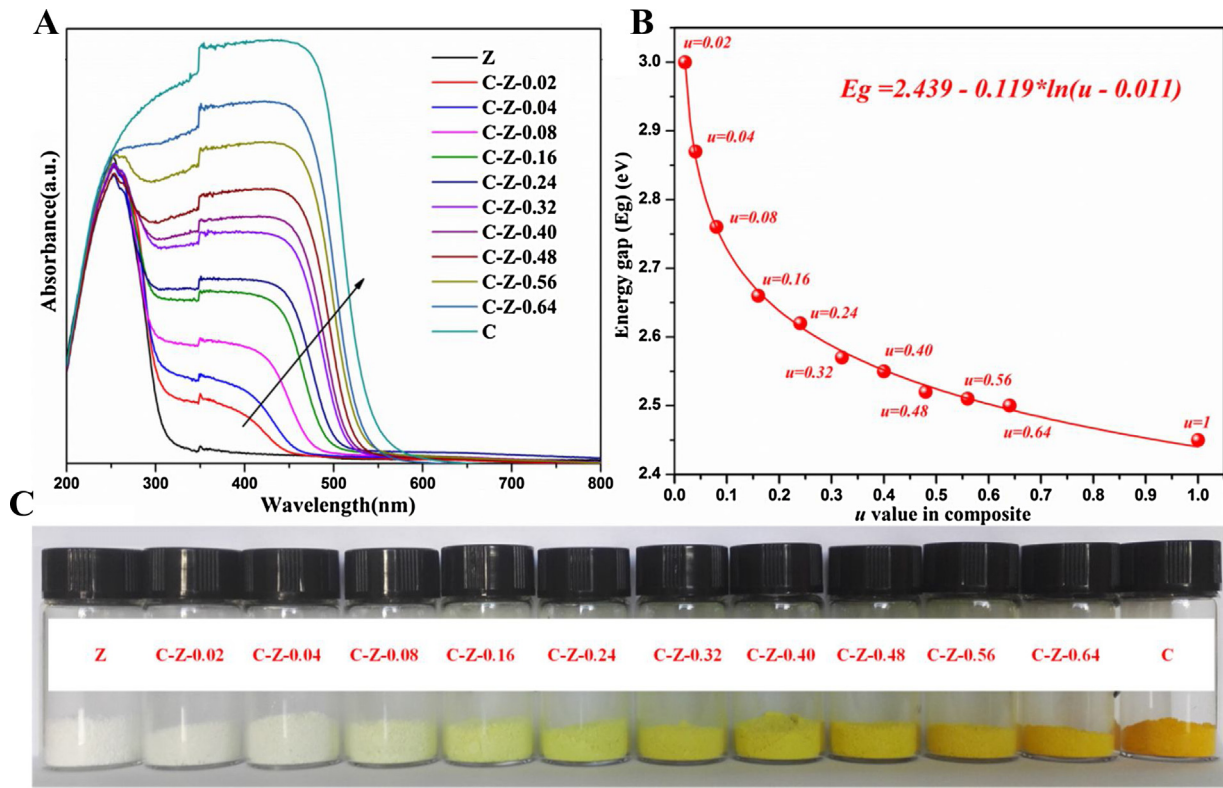


Fig. 2. UV-vis DRS of the as-obtained samples (A). A nonlinearly relationship of E_g of $Zn_{1-x}Cd_xS$ in C-Z- u hybrids as a function of u value (B). Color photographs of all samples (C).

that of pristine Z and C sample, respectively. The corresponding apparent quantum efficiency (AQY) of C-Z-0.24 reaches up to 49.95% at 440 nm. Even under illumination of the natural sunlight (Fuzhou City, 15:20 ~ 15:30 p.m., Mar. 1, 2017) or visible-light irradiation ($\lambda > 420$ nm) and at ambient pressure, gas-bubble formation is observed over C-Z-0.24 sample, as recorded in Movie S1 and S2. The ambient temperature was recorded about 20 °C. Detailed photocatalytic experiments are displayed in Fig. S1. Though, C-Z- u sample exhibits the increasing absorbance as the u value increases in Fig. 2A. C-Z-0.24 sample, with a relatively low absorbance, exhibits the best photocatalytic performance. These are the possible reasons: On one hand, the absorbance of C-Z- u sample enhances as the u value increases. On the other hand, With the increasing u value, the lattice constant c of $Zn_{1-x}Cd_xS$ increases gradually, decreasing lattice matching between $Zn_{1-x}Cd_xS$ and ZnS slices in $ZnS(en)_{0.5}$. And, the CB edge potential becomes more negative, decreasing the band structure matching. Though the enhanced absorbance could improve photoactivity, the increased lattice stress and band structure mismatch would decrease interfacial carriers separation efficiency, leading to a lower photoactivity. Thus, the u value in C-Z- u sample may be not proportioned to the photocatalytic performance in the whole range of 0 ~ 1. The optimized u value should balance the absorbance and lattice and band structure matching well to ensure a superior photocatalytic performance. Therefore, the superior photoactivity of C-Z-0.24 sample could be associated with the formation of the perfect heterojunctions with suitable lattice parameter and energy band structure, based on the controllable composition promoting surface carriers separation. Meanwhile, 1D/2D hierarchical nanostructure may facilitate the carriers migration from bulk to interface. Moreover, in order to embody the superiority of $Zn_{1-x}Cd_xS/D-ZnS(en)_{0.5}$ heterojunction, we also prepared pure $Zn_{0.41}Cd_{0.59}S$ sample via a solvothermal method previously reported [75]. The detailed synthetic processes are presented in Supporting Information. The XRD pattern and SEM

image of $Zn_{0.41}Cd_{0.59}S$ sample as displayed in Fig. S2A, indicate the successful synthesis of $Zn_{0.41}Cd_{0.59}S$ nanorods. Then, the photocatalytic H_2 production activity of $Zn_{0.41}Cd_{0.59}S$ is also investigated. As shown in Fig. S2B, the photocatalytic H_2 evolution rate is about 46.2 $\mu\text{mol H}^{-1}$ per 30 mg $Zn_{0.41}Cd_{0.59}S$ sample, which is about 2.37 times the H_2 evolution rate of C sample, and lower than a tenth of that of $Zn_{0.41}Cd_{0.59}S/D-ZnS(en)_{0.5}$ hybrid. These results imply that the perfect $Zn_{0.41}Cd_{0.59}S/D-ZnS(en)_{0.5}$ heterojunctions dominantly contribute to the superior photoactivity of C-Z-0.24 sample. Therefore, this unique 1D/2D heterostructure with much perfect heterojunctions could provide effective carriers transport channels both in the bulk and interface, and achieve a boost in photocatalytic performance. This assumption is further verified by transient photocurrent experiments and electrochemical impedance spectroscopy (EIS) Nyquist plots. As shown in Fig. 6B, Z sample shows a weak photocurrent response under visible-light irradiation due to the limited visible-light absorption. In the case of C sample, a cathode current spike occurs at the initial time of irradiation, and then the photocurrent declines sharply over time to a relatively steady photocurrent. Such obvious current decay indicates serious photoexcited carriers recombination in CdS. Yet for C-Z-0.24 hybrid, the transient photocurrent response gradually increases as prolonging light exposure time and eventually reaches a constant value. This steady photocurrent response of C-Z-0.24 composite is much stronger than ones of Z and C samples. Furthermore, the photocurrent intensity of C-Z-0.24 sample decays much slower than those of Z and C samples after stopping irradiation. It demonstrates that the carrier lifetime in C-Z-0.24 heterostructure is much longer. On the other hand, C-Z-0.24 composite exhibits a smallest semicircular arc in the EIS spectrum (Fig. 6C). These photoelectrochemical measurements indeed reveal a high-efficiency carriers separation existing in C-Z-0.24 hybrid. Besides, it is well-known that large surface area not only can provide more active sites, but also can promote the carriers separation by decreasing the trans-

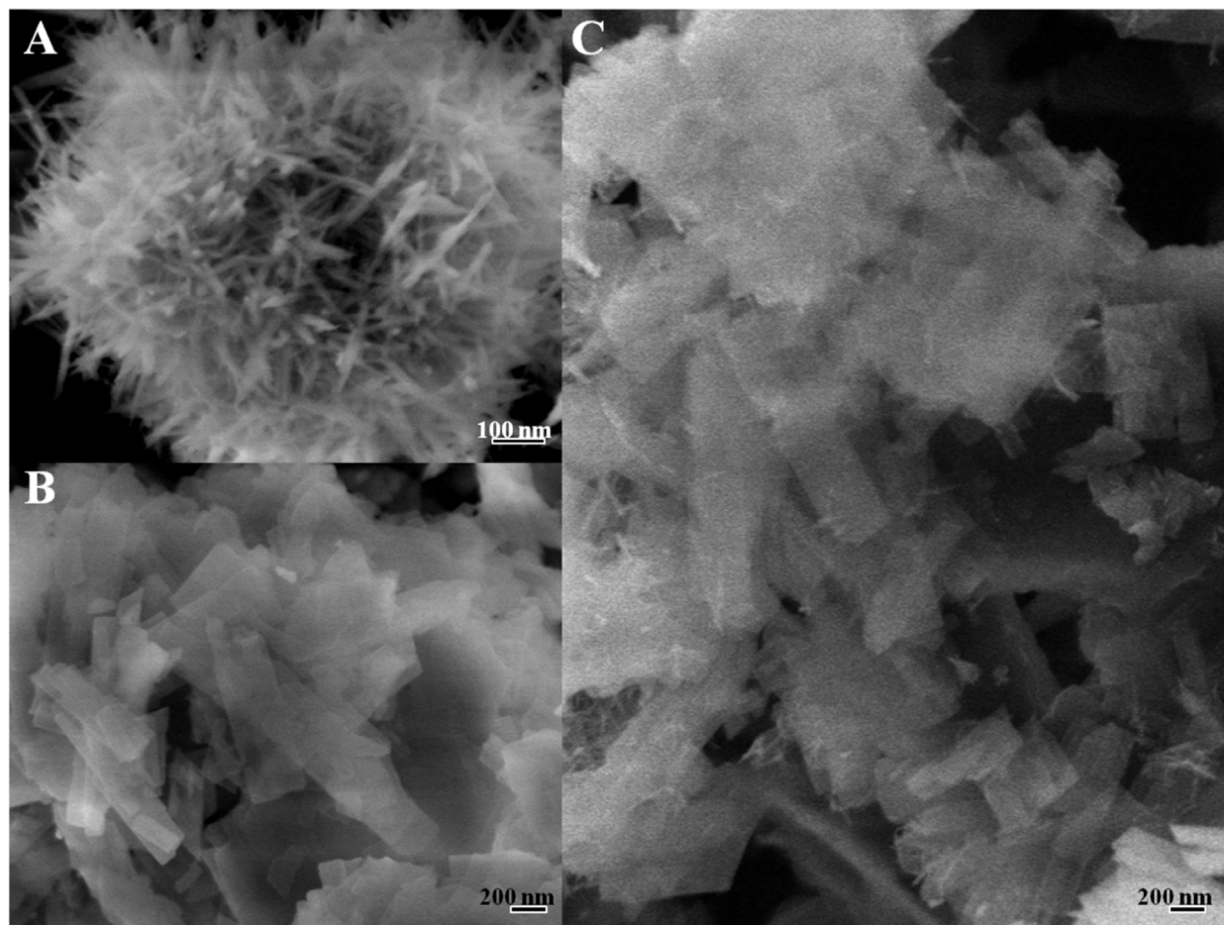


Fig. 3. SEM images of the pristine CdS (A), D-ZnS(en)_{0.5} (B) and C-Z-0.24 composite (C).

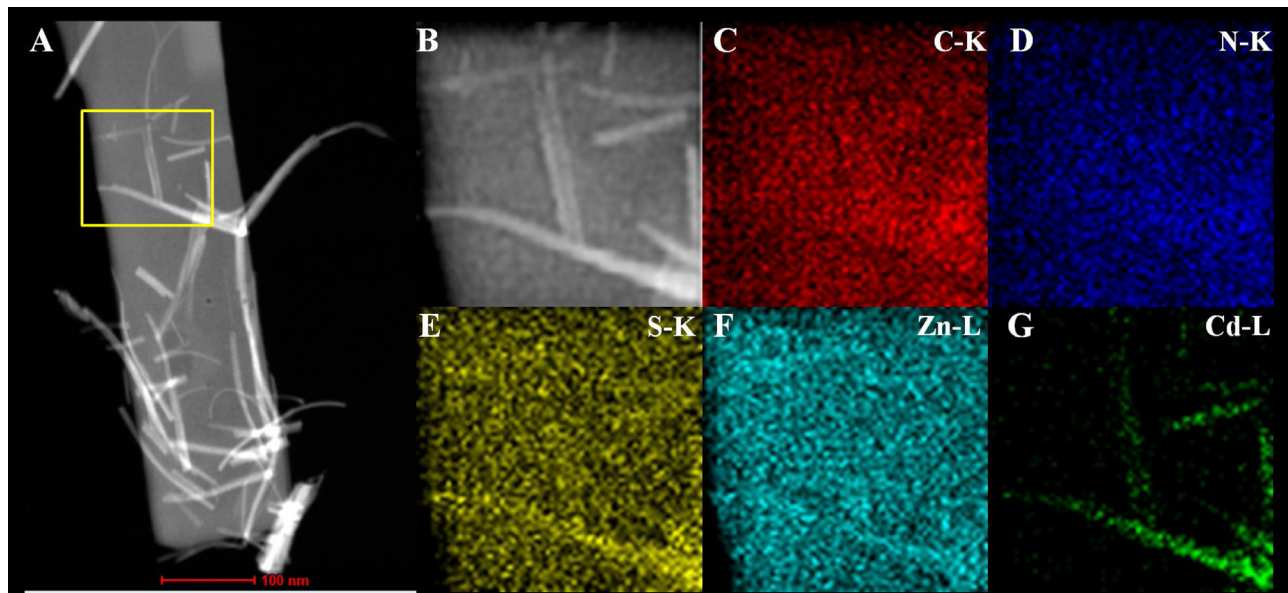


Fig. 4. HAADF-STEM (A, B) and EDX-STEM elemental mapping images of C-Z-0.24 sample.

mission distance of photoinduced hole/electron pairs. Therefore, nitrogen adsorption/desorption isotherms and the corresponding pore size distribution curves of Z, C and C-Z-0.24 samples are also displayed in Fig. 6D and E. As shown, C-Z-0.24 hybrid possesses the largest specific surface area (S_{BET}) of $67.5 \text{ m}^2 \text{ g}^{-1}$, with mesopores

($2\text{--}50 \text{ nm}$) and macropores ($50\text{--}100 \text{ nm}$) structure. Though the S_{BET} of C-Z-0.24 sample is larger than that of Z ($17.5 \text{ m}^2 \text{ g}^{-1}$) and C sample ($49.8 \text{ m}^2 \text{ g}^{-1}$), the hydrogen production rate of C-Z-0.24 sample normalized by surface area is still markedly higher than ones of Z and C samples (inset in Fig. 6D) Thus, it is further confirmed that

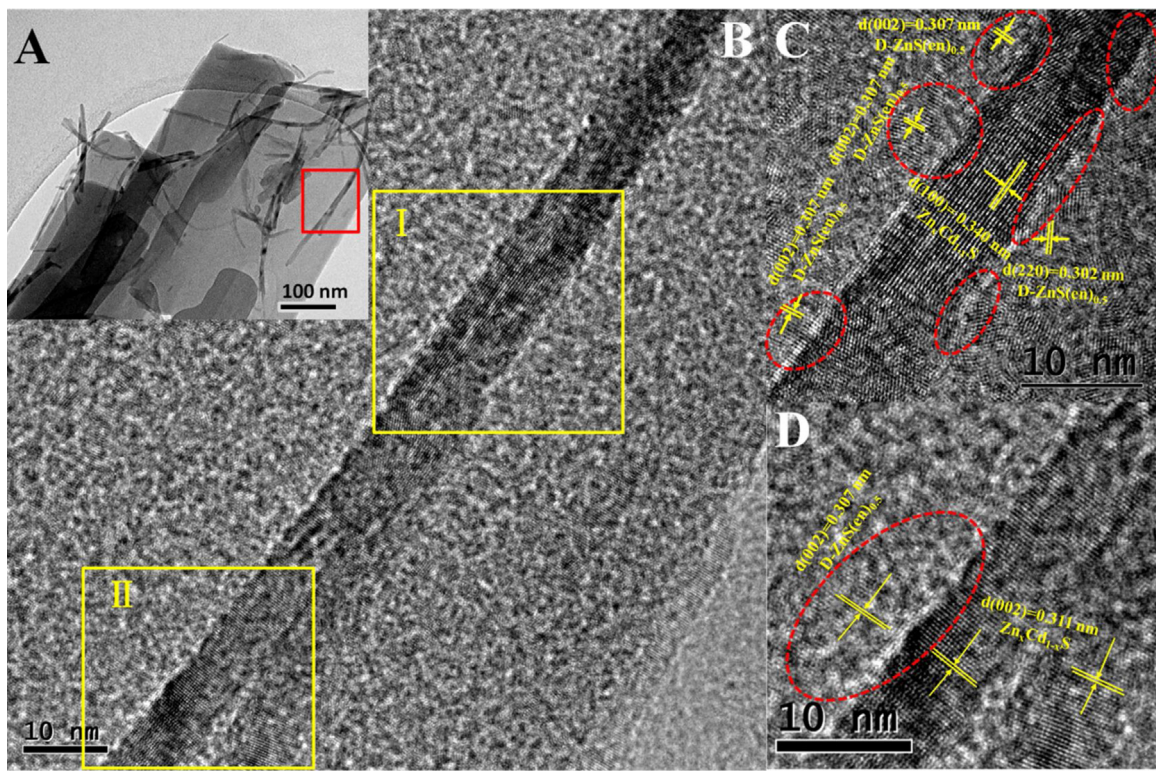


Fig. 5. TEM (A) and HRTEM (B-D) images of C-Z-0.24 heterostructure.

the significantly improved carrier separation rate is dominantly attributed to the perfect heterojunctions in well-defined 1D/2D heterostructure.

What's more, each component content in C-Z-0.24 composite is determined by means of TGA. Fig. 6F displays the TGA analytic result of Z, C and C-Z-0.24 samples in N₂ surrounding with a heating rate of 10 °C•min⁻¹. For C sample, only a slight weight loss in the test temperature range (25–700 °C). It might be mainly caused by the elimination of absorbed water on the surface of C sample in the range of 25–300 °C, and the slight oxidation of CdS in the range of 300–700 °C. While there are three weight loss stages in the measurement range for both Z and C-Z-0.24 samples. The first weight loss before 300 °C is mainly because of the elimination of absorbed water on the surface of Z or C-Z-0.24 sample. The second obviously weight loss process is from 300 to 420 °C, resulting from the decomposition of en in Z sample. The weight loss in this stage can be ascribed to the conversion from ZnS(en)_{0.5} to ZnS. The net weight loss of the pure Z sample is about 22 wt% in this stage, which is very close to the reported experimental results [76–79]. In contrast, the net weight loss for C-Z-0.24 hybrid is ca. 15 wt% in this stage. Therefore, the mass ratio of Zn_{1-x}Cd_xS/D-ZnS(en)_{0.5} could be derived based on the following equation:

$$\frac{m_Z \times 22\text{wt}\%}{(m_Z + m_{Zn1-xCd_xS})} = 15\text{wt}\% \quad (1)$$

Where m_Z and $m_{Zn1-xCd_xS}$ are the masses of D-ZnS(en)_{0.5} and Zn_{1-x}Cd_xS in C-Z-0.24 composite respectively. As estimated, the approximate mass ratio of Zn_{1-x}Cd_xS/D-ZnS(en)_{0.5} in C-Z-0.24 composite is 7:8. Besides, the third weight loss after 420 °C is very slight, which might stem from the partial S atoms are replaced by O atoms. More specifically, the corresponding x value of Zn_{1-x}Cd_xS in C-Z-0.24 sample is about 0.59 (Fig. 1C). That is, C-Z-0.24 sample represents the hybrid of Zn_{0.41}Cd_{0.59}S/D-ZnS(en)_{0.5} with the mass ratio of 7:8. and Eg value of Zn_{0.41}Cd_{0.59}S is ca. 2.62 eV (Fig. 2B). Further, on the one hand, the CB potential of Zn_{0.41}Cd_{0.59}S is speculated to

be about –0.36 V vs. NHE following the previous literature [29], and the VB potential of that is calculated to be +2.26 V vs. NHE. On the other hand, due to the enriched defect structures in D-ZnS(en)_{0.5} whose CB located at about –1.0 V vs. NHE, a deep p-type defect energy level posited at ca. +0.80 V vs. NHE is created as our previous report [73]. The enriched defects not only can induce intraband transition under visible light irradiation, but also can mediate the formation of the staggered energy band alignment from straddling energy band alignment of Zn_{0.41}Cd_{0.59}S/D-ZnS(en)_{0.5}. Based on the lattice-matched and band-matched Zn_{0.41}Cd_{0.59}S/D-ZnS(en)_{0.5} heterojunctions, the superior photocatalytic H₂ evolution mechanism of C-Z-0.24 heterostructure under visible light irradiation is demonstrated as Scheme 1. As depicted, both intrinsic excitation of Zn_{0.41}Cd_{0.59}S and intraband transition in D-ZnS(en)_{0.5} are induced under visible light irradiation, generating free electrons on CB and holes on VB or defect level of both components. Driven by the potential difference of CB of both components and potential difference between VB of Zn_{0.41}Cd_{0.59}S and defect level of D-ZnS(en)_{0.5}, consequently, the photoexcited electrons transfer from the CB of D-ZnS(en)_{0.5} into the CB of Zn_{0.41}Cd_{0.59}S, and holes migrate from the VB of Zn_{0.41}Cd_{0.59}S into the defect level of D-ZnS(en)_{0.5} inversely. Thus the effective carriers spatial separation is achieved. Finally, the separated electrons in CB of Zn_{0.41}Cd_{0.59}S and holes on the defect level of D-ZnS(en)_{0.5} participate in reducing H⁺ into H₂ and oxidizing the sacrificial reagents, respectively.

In addition, the photostability of photocatalyst is known as another important indicator for practical photocatalytic application. Therefore, the stability of C-Z-0.24 hybrid is also investigated. Fig. 7A reveals that C-Z-0.24 composite still maintained 64% of the original photocatalytic activity after six consecutive runs without any recovery of the reagents and photocatalyst, though a total of 9.65 mmol H₂ are produced over 30 mg C-Z-0.24 catalyst under visible light irradiation. Furthermore, both the crystalline structure and microstructure of C-Z-0.24 hybrid don't change obviously undergoing photocatalytic reaction for 24 h as exhibited in

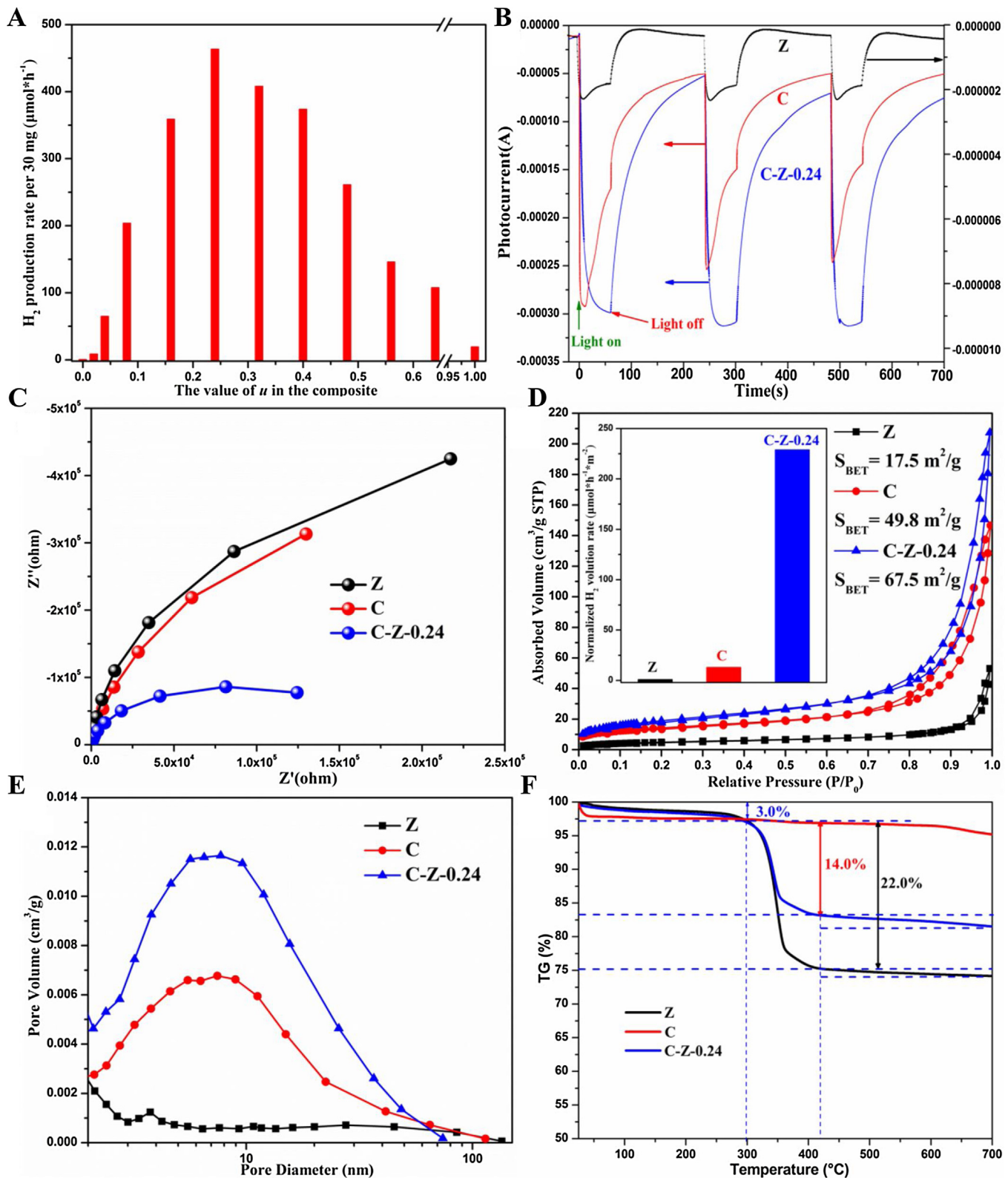
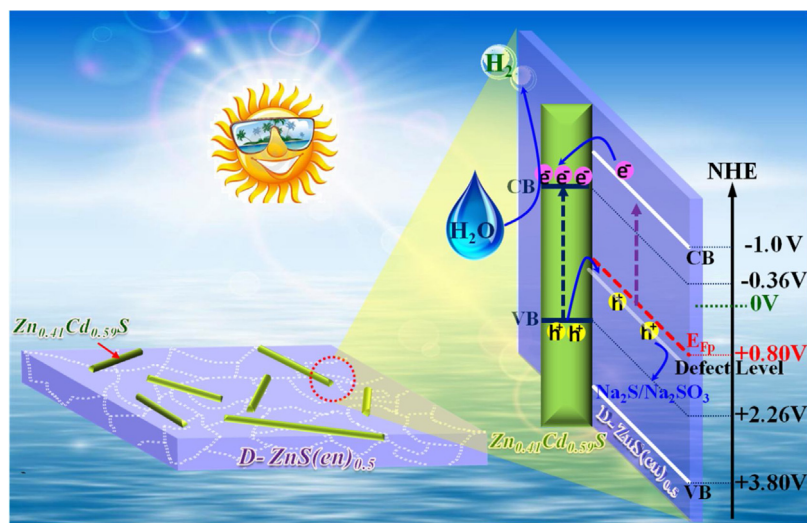


Fig. 6. Photocatalytic H₂ evolution rates of all samples under visible light irradiation ($\lambda > 420$ nm) (A). Comparison of photocurrents (B) and EIS spectra (C) of Z, C and C-Z-0.24 samples. N₂ absorption-desorption isotherms (D) and the corresponding pore size distribution curves (E) of Z, C and C-Z-0.24 samples (inset: Normalized H₂ evolution rates of Z, C and C-Z-0.24 samples). TGA curves of Z, C and C-Z-0.24 samples (F).

Fig. 7B-D. In Fig. 7C and D, it seems to be found that the contact between Zn_{1-x}Cd_xS and D-ZnS(en)_{0.5} maybe weaker in the used C-Z-0.24 hybrid. This weakened contact could hinder carriers interface transfer, resulting the attenuation of photocatalytic

H₂ evolution. Through further comparing the TG curves of the fresh and used C-Z-0.24 samples in Fig. 8A, it is found that some changes in the weight loss process come after photocatalytic reaction for 24 h. Firstly, the weight loss from 25 to 300 °C for used C-Z-0.24



Scheme 1. Schematic illustration of the migration and transportation of photogenerated carriers in C-Z-0.24 heterojunction during the visible-light-driven photocatalytic reaction for H_2 production from water.

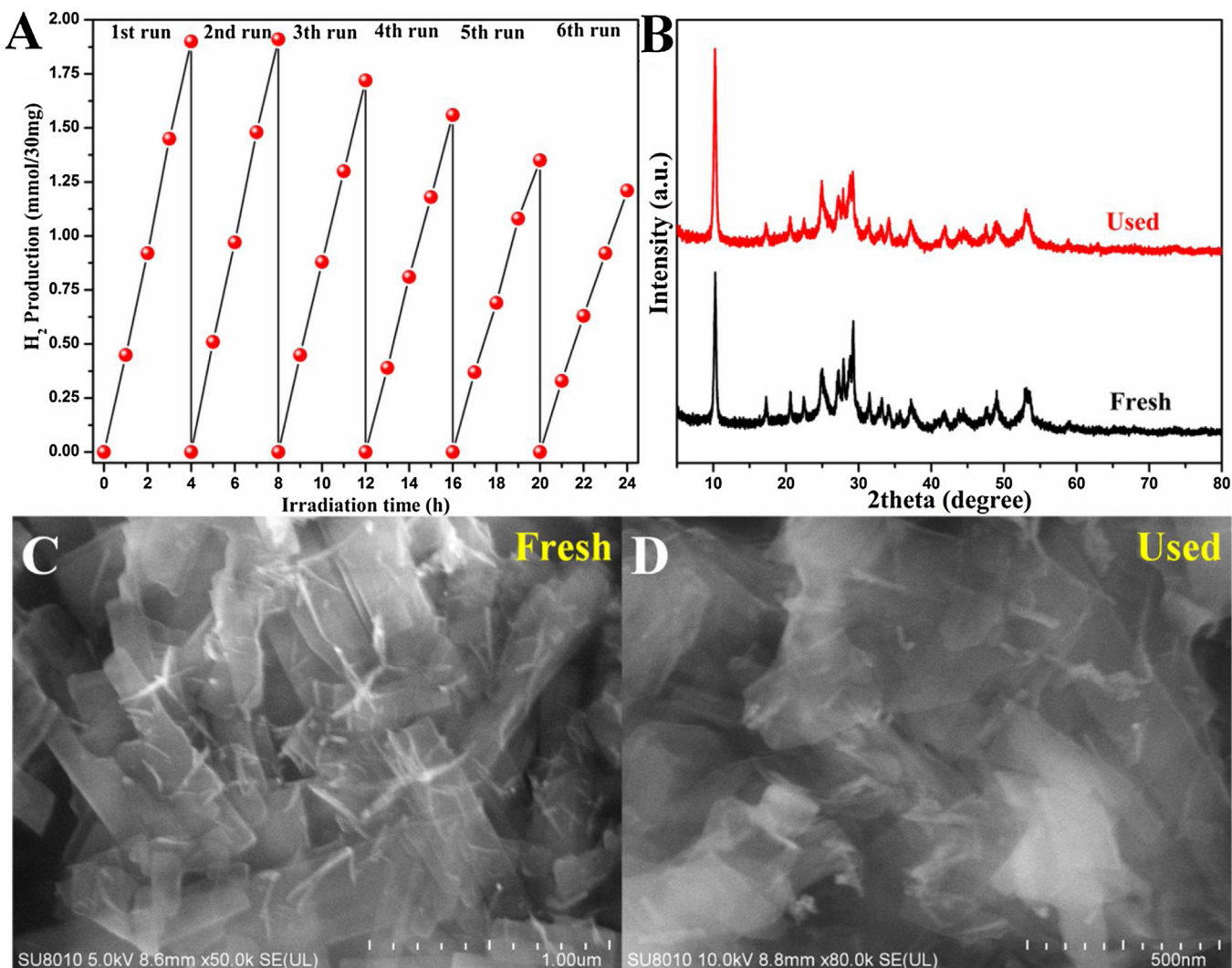


Fig. 7. Time courses of H_2 production over C-Z-0.24 composite under visible light irradiation ($\lambda > 420$ nm) (A). XRD patterns of C-Z-0.24 before and after visible light irradiation for 24 h in Na_2S (0.35 M) and Na_2SO_3 (0.25 M) aqueous solution (B). SEM images of fresh (C) and used (D) C-Z-0.24 sample.

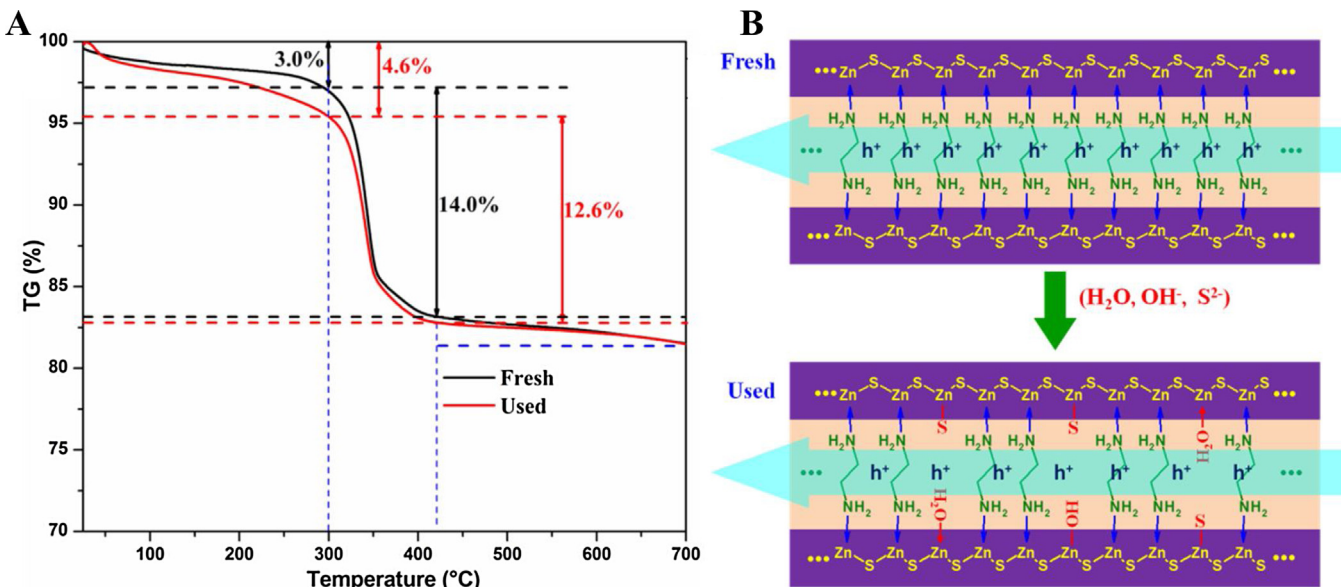


Fig. 8. TGA curves of the fresh and used C-Z-0.24 sample (A). The scheme illustrating the probable changes in C-Z-0.24 before and after visible light irradiation for 24 h in Na₂S (0.35 M) and Na₂SO₃ (0.25 M) aqueous solution (B).

sample is about 4.6 wt%, which is higher than that of fresh C-Z-0.24 sample (3.0 wt%). It indicates that more absorbed water exists in the used sample. Secondly, the weight loss from 300 to 420 °C decreases to 12.6 wt% after 24 h of photocatalytic reaction. These phenomena are probably caused by the following two steps during the photocatalytic process: (i) Some en molecules are dissociated, decreasing the content of en and inducing the generation of some unsaturated Zn²⁺ in C-Z-0.24 sample. (ii) Some of the induced unsaturated Zn²⁺ are subsequently coordinated by H₂O molecules or OH⁻ anions. Thirdly, it is also remarkable that the residual weight for both samples are the same. It demonstrates that some S²⁻ anions also could exchange with en molecules, on account of the relative molecular mass of (en)_{0.5}, which is higher than H₂O or OH⁻ and less than S²⁻. Overall, partial en ligands could be dissociated or substituted by H₂O, OH⁻, and S²⁻ in our photocatalytic reaction system. It would make the consecutive conduction pathway for holes become intermittent as displayed in Fig. 8B, decelerating the hole transfer in ZnS(en)_{0.5}.

In order to further reveal the variation of structure and composition for C-Z-0.24 hybrid before and after reaction, X-ray photoemission spectroscopy (XPS) analysis is also conducted. Fig. 9 presents the XPS spectra of both fresh and used C-Z-0.24 sample. In Zn 2p spectra of C-Z-0.24 composite (Fig. 9A), two peaks at 1021.9 and 1045.0 eV could be assigned to Zn 2p_{5/2} and 2p_{3/2} of Zn²⁺ in the fresh sample [80]. While the peaks corresponding to Zn 2p_{5/2} and 2p_{3/2} shift toward higher binding energy (BE) (1022.3 and 1045.4 eV), after photocatalytic reaction for 24 h. The possible causes are that abundant H₂O, S²⁻, and OH⁻ ions bond with the unsaturated Zn²⁺ ions after the dissociation of en, leading to the elimination of S²⁻ vacancy or unsaturated Zn²⁺ and formation of more Zn-S and Zn-O bonds. Compared with the Zn 2p spectra of D-ZnS(en)_{0.5}, the disappearance of the two peaks corresponding to defect-induced Zn-involving species may be due to the lower content in C-Z-0.24 sample [73]. As shown in Fig. 9B, two deconvoluted N 1s XPS peaks at 399.4 and 400.7 eV may be attributed to the Zn-N bond in [Zn ← (en)_{0.5}]²⁺ and [(en)_{0.5} → Zn ← (en)_{0.5}]²⁺ group respectively [73]. The BE values of both N 1s peaks are ~0.10 eV less than that of N 1s peaks in pure D-ZnS(en)_{0.5}. This further indicates the strong interaction between D-ZnS(en)_{0.5} and Zn_{1-x}Cd_xS. However, only one peak at 399.9 eV, derived from [Zn ← (en)_{0.5}]²⁺ group, presents in the used C-Z-0.24. The disappearance of the peak

originated from $[(\text{en})_{0.5} \rightarrow \text{Zn} \leftarrow (\text{en})_{0.5}]^{2+}$ group may result from the priority dissociation of en in $[(\text{en})_{0.5} \rightarrow \text{Zn} \leftarrow (\text{en})_{0.5}]^{2+}$ group, and the higher BE of Zn-N in $[\text{Zn} \leftarrow (\text{en})_{0.5}]^{2+}$ group may arise from the occurrence of ligand exchange between $\text{H}_2\text{O}/\text{OH}^-$ and en. As for the Cd 3d XPS spectra of the fresh C-Z-0.24 sample, two peaks at higher BE (405.5 and 412.2 eV) could be contributed from Cd^{2+} in $\text{Zn}_{1-x}\text{Cd}_x\text{S}$, and the other two peaks at 404.6 and 411.3 eV could be assigned to Cd in a lower valence state, which might result from sulfur vacancies on the surface of $\text{Zn}_{1-x}\text{Cd}_x\text{S}$ [81,82]. By contrast, only a set of peaks at 405.3 and 412.0 eV corresponding to Cd^{2+} exists in $\text{Zn}_{1-x}\text{Cd}_x\text{S}$, and the peak shifting toward lower BE indicates that the partial oxidation of Cd-S induces the formation of Cd-O bond on the surface of $\text{Zn}_{1-x}\text{Cd}_x\text{S}$ [83]. Meanwhile, the another set of peaks disappears with the repair of S vacancies during the photocatalytic process. Remarkably, the peak shift of 0.5 eV toward higher BE can also be found in S 2p XPS spectra, that would further demonstrate the partial oxidation of Cd-S bonds, forming O–Cd–S species on the surface of $\text{Zn}_{1-x}\text{Cd}_x\text{S}$. Above XPS results are in consistent with TG results. Moreover, the repair of S vacancies and partial oxidation of Cd-S bonds on the surface of $\text{Zn}_{1-x}\text{Cd}_x\text{S}$ could also accompany with photocatalytic reaction. In all, we suggest several possible causes to lead a loss of ca. 36% of photoactivity for C-Z-0.24 composite. On one hand, partial en ligands are dissociated or substituted by H_2O , OH^- and S^{2-} , that would make the consecutive conduction pathway for holes become intermittent, decelerating the hole transfer in $\text{ZnS}(\text{en})_{0.5}$. On the other hand, the repair of S vacancies and partial oxidation of Cd-S bonds on the surface of $\text{Zn}_{1-x}\text{Cd}_x\text{S}$ could also weaken the photocatalytic performance due to the reduction of defect-induced exciton. Besides, the weakened contact could also hinder carriers interface transfer, resulting the attenuation of photocatalytic H_2 evolution. These possibilities are further evidenced by transient photocurrent and EIS measurements. Indeed, the charge transfer resistance of C-Z-0.24 sample increases and the photocurrent response intensity decrease after photocatalytic reaction as exhibited in Fig. 10.

4. Conclusions

In summary, a series of 1D/2D $Zn_{1-x}Cd_x/D-ZnS(en)_{0.5}$ heterostructures have been fabricated successfully by a facile one-pot

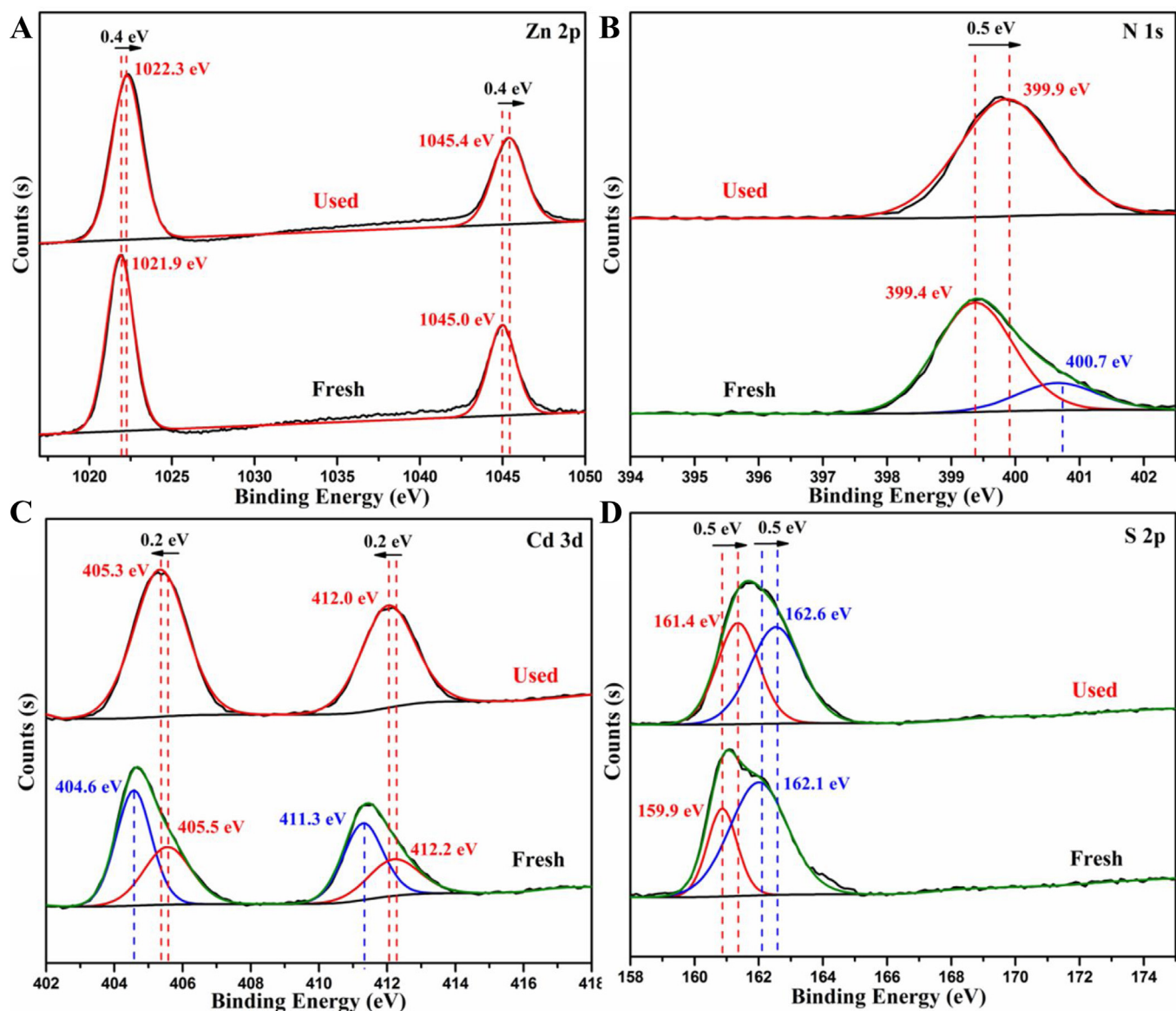


Fig. 9. XPS spectra of Zn 2p (A), N 1s (B), Cd 3d (C) and S 2p (D) of C-Z-0.24 sample without and after visible light irradiation for 24 h in Na₂S (0.35 M) and Na₂SO₃ (0.25 M) aqueous solution.

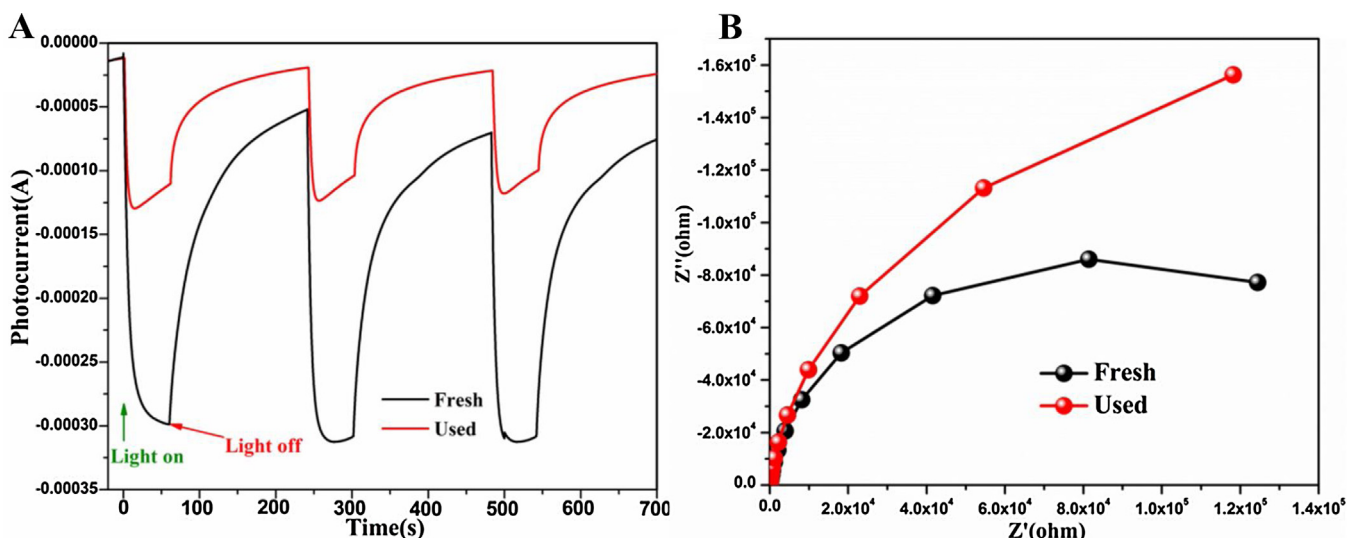


Fig. 10. Comparison of photocurrents (A) and EIS spectra (B) of fresh and used C-Z-0.24 sample.

solvothermal method. The heterojunctions with well-matched lattice and band structure at the interface are constructed, based on the dual regulation of composition and defect, which facilitates the interfacial carriers separation. Meanwhile, the interior carriers migration can be promoted by controlling of dimensions. Owing to the synergistic optimization of interior and interfacial carriers separation, the photocatalytic performance of $Zn_{1-x}Cd_x/D-ZnS(en)_{0.5}$ samples are improved significantly. The optimal $Zn_{0.41}Cd_{0.59}S/D-ZnS(en)_{0.5}$ heterostructure, with the mass ratio of 7:8, shows an extremely high photocatalytic H_2 production rate of $463.6 \mu\text{mol H}^{-1}$ per 30 mg under visible light irradiation ($\lambda > 420 \text{ nm}$), which is about 826 and 24 times higher than that of pristine D-ZnS(en)_{0.5} and CdS, respectively. Besides, the apparent quantum yield (AQY) at 440 nm reaches up to 49.95%. In addition, some possible causes of performance degradation for $Zn_{0.41}Cd_{0.59}S/D-ZnS(en)_{0.5}$ sample also are revealed by SEM, TGA and XPS analysis. Those are the weakened interfacial contact, partial en ligands dissociation and substitution by H_2O , OH^- and S^{2-} in D-ZnS(en)_{0.5}, repair of S vacancies and partial oxidation of Cd-S bonds on the surface of $Zn_{1-x}Cd_xS$.

Acknowledgements

This work is supported by the National Key Technologies R & D Program of China (2014BAC13B03), the funding under National Natural Science Foundation of China (21473031, 21673041), the National Basic Research Program of China (973 Program: 2013CB632405), and the Science & Technology Plan Project of Fujian Province (2014Y2003), and support from Natural Science Foundation of Fujian Province (2016J01693).

Appendix A. Supplementary data

Supplementary data associated with this article can be found, in the online version, at <http://dx.doi.org/10.1016/j.apcatb.2017.08.002>.

References

- [1] A. Kudo, Y. Miseki, Chem. Soc. Rev. 38 (2009) 253–278.
- [2] J. Ran, J. Zhang, J. Yu, M. Jaroniec, S.Z. Qiao, Chem. Soc. Rev. 43 (2014) 7787–7812.
- [3] Y. Xu, M. Kraft, R. Xu, Chem. Soc. Rev. 45 (2016) 3039–3052.
- [4] X. Zou, Y. Zhang, Chem. Soc. Rev. 44 (2015) 5148–5180.
- [5] J. Ran, J. Zhang, J. Yu, M. Jaroniec, S.Z. Qiao, Chem. Soc. Rev. 43 (2014) 7787–7812.
- [6] S.J.A. Moniz, S.A. Shevlin, D.J. Martin, Z.-X. Guo, J. Tang, Energy Environ. Sci. 8 (2015) 731–759.
- [7] S. Linic, P. Christopher, D.B. Ingram, Nat. Mater. 10 (2011) 911–921.
- [8] P. Kalisman, Y. Nakibli, L. Amirav, Nano Lett. 16 (2016) 1776–1781.
- [9] C. Pan, T. Takata, M. Nakabayashi, T. Matsumoto, N. Shibata, Y. Ikuhara, K. Domen, Angew. Chem. Int. Ed. 54 (2015) 2955–2959.
- [10] Q. Wang, T. Hisatomi, Y. Suzuki, Z. Pan, J. Seo, M. Katayama, T. Minegishi, H. Nishiyama, T. Takata, K. Seki, A. Kudo, T. Yamada, K. Domen, J. Am. Chem. Soc. 139 (2017) 1675–1683.
- [11] K. Maeda, K. Domen, J. Phys. Chem. Lett. 1 (2010) 2655–2661.
- [12] Q. Wang, T. Hisatomi, Q. Jia, H. Tokudome, M. Zhong, C. Wang, Z. Pan, T. Takata, M. Nakabayashi, N. Shibata, Y. Li, I.D. Sharp, A. Kudo, T. Yamada, K. Domen, Nat. Mater. 15 (2016) 611–615.
- [13] L. Liao, Q. Zhang, Z. Su, Z. Zhao, Y. Wang, Y. Li, X. Lu, D. Wei, G. Feng, Q. Yu, X. Cai, J. Zhao, Z. Ren, H. Fang, F. Robles-Hernandez, S. Baldelli, J. Bao, Nat. Nanotechnol. 9 (2014) 69–73.
- [14] K. Maeda, K. Teramura, D. Lu, T. Takata, N. Saito, Y. Inoue, K. Domen, Nature 440 (2006) 295–295.
- [15] J. Chen, C.L. Dong, D. Zhao, Y.C. Huang, X. Wang, L. Samad, L. Dang, M. Shearer, S. Shen, L. Guo, Adv. Mater. 29 (2017) 1606198.
- [16] C. Pan, T. Takata, K. Domen, Chem. Eur. J. 22 (2016) 1854–1862.
- [17] J. Liu, Y. Liu, N. Liu, Y. Han, X. Zhang, H. Huang, Y. Lifshitz, S.T. Lee, J. Zhong, Z. Kang, Science 347 (2015) 970–974.
- [18] J. Chen, F. Qiu, W. Xu, S. Cao, H. Zhu, Appl. Catal. A: General 495 (2015) 131–140.
- [19] H.M. Chen, C.K. Chen, R.-S. Liu, L. Zhang, J. Zhang, D.P. Wilkinson, Chem. Soc. Rev. 41 (2012) 5654.
- [20] Q. Xiang, J. Yu, J. Phys. Chem. Lett. 4 (2013) 753–759.
- [21] A.B. Djurišić, Y.H. Leung, A.M. Ching Ng, Mater. Horiz. 1 (2014) 400.
- [22] H. Wang, L. Zhang, Z. Chen, J. Hu, S. Li, Z. Wang, J. Liu, X. Wang, Chem. Soc. Rev. 43 (2014) 5234–5244.
- [23] F. Dong, Z. Zhao, T. Xiong, Z. Ni, W. Zhang, Y. Sun, W.K. Ho, ACS Appl. Mater. Inter. 5 (2013) 11392–11401.
- [24] K. Li, R. Chen, S.-L. Li, M. Han, S.-L. Xie, J.-C. Bao, Z.-H. Dai, Y.-Q. Lan, Chem. Sci. 6 (2015) 5263–5268.
- [25] N. Zhang, M.Q. Yang, Z.R. Tang, Y.J. Xu, ACS nano 8 (2014) 623–633.
- [26] S. Weng, Z. Fang, Z. Wang, Z. Zheng, W. Feng, P. Liu, ACS Appl. Mater. Inter. 6 (2014) 18423–18428.
- [27] J. Zhang, M. Zhang, R.-Q. Sun, X. Wang, Angew. Chem. Int. Ed. 51 (2012) 10145–10149.
- [28] K. Li, R. Chen, S.L. Li, S.L. Xie, L.Z. Dong, Z.H. Kang, J.C. Bao, Y.Q. Lan, ACS Appl. Mater. Inter. 8 (2016) 14535–14541.
- [29] Q. Li, H. Meng, P. Zhou, Y. Zheng, J. Wang, J. Yu, J. Gong, ACS Catal. 3 (2013) 882–889.
- [30] Q. Li, H. Meng, J. Yu, W. Xiao, Y. Zheng, J. Wang, J. ChemEur. (2014) 1176–1185.
- [31] J. Zhang, J. Yu, M. Jaroniec, J.R. Gong, Nano Lett. 12 (2012) 4584–4589.
- [32] Y. Hao, S.-Z. Kang, X. Liu, X. Li, L. Qin, J. Mu, ACS Sustain. Chem. Eng. 5 (2017) 1165–1172.
- [33] M. Liu, Y. Chen, J. Su, J. Shi, X. Wang, L. Guo, Nat. Energy 1 (2016) 16151.
- [34] M. Liu, L. Wang, G. Lu, X. Yao, L. Guo, Energy Environ. Sci. 4 (2011) 1372.
- [35] X. Xu, R. Lu, X. Zhao, S. Xu, X. Lei, F. Zhang, D.G. Evans, Appl. Catal. B: Environ. 102 (2011) 147–156.
- [36] H. Du, K. Liang, C.Z. Yuan, H.L. Guo, X. Zhou, Y.F. Jiang, A.W. Xu, ACS Appl. Mater. Inter. 8 (2016) 24550–24558.
- [37] Y.Y. Hsu, N.T. Suen, C.C. Chang, S.F. Hung, C.L. Chen, T.S. Chan, C.L. Dong, C.C. Chan, S.Y. Chen, H.M. Chen, ACS Appl. Mater. Inter. 7 (2015) 22558–22569.
- [38] J. Song, H. Zhao, R. Sun, X. Li, D. Sun, Energy Environ. Sci. 10 (2017) 225–235.
- [39] S.N. Guo, Y.L. Min, J.C. Fan, Q.J. Xu, ACS Appl. Mater. Inter. 8 (2016) 2928–2934.
- [40] J. Zhang, L. Qi, J. Ran, J. Yu, S.Z. Qiao, Adv. Energy Mater. 4 (2014) 1301925.
- [41] H. Shen, X. Bai, A. Wang, H. Wang, L. Qian, Y. Yang, A. Titov, J. Hyvonen, Y. Zheng, L.S. Li, Adv. Funct. Mater. 24 (2014) 2367–2373.
- [42] Y. Lu, D. Wang, P. Yang, Y. Du, C. Lu, Catal. Sci. Technol. 4 (2014) 2650.
- [43] X. Guo, Y. Chen, Z. Qin, M. Wang, L. Guo, Int. J. Hydrogen Energy 41 (2016) 15208–15217.
- [44] N. Li, B. Zhou, P. Guo, J. Zhou, D. Jing, Int. J. Hydrogen Energy 38 (2013) 11268–11277.
- [45] Y. Chen, S. Zhao, X. Wang, Q. Peng, R. Lin, Y. Wang, R. Shen, X. Cao, L. Zhang, G. Zhou, J. Li, A. Xia, Y. Li, J. Am. Chem. Soc. 138 (2016) 4286–4289.
- [46] H.-L. Guo, H. Du, Y.-F. Jiang, N. Jiang, C.-C. Shen, X. Zhou, Y.-N. Liu, A.-W. Xu, J. Phys. Chem. C 121 (2017) 107–114.
- [47] J. Xu, X. Yang, H. Wang, X. Chen, C. Luan, Z. Xu, Z. Lu, V.A. Roy, W. Zhang, C.S. Lee, Nano Lett. 11 (2011) 4138–4143.
- [48] S. Chakrabarty, K. Chakraborty, A. Laha, T. Pal, S. Ghosh, J. Phys. Chem. C 118 (2014) 28283–28290.
- [49] J. Zhang, Q. Xu, S.Z. Qiao, J. Yu, ChemSusChem 6 (2013) 2009–2015.
- [50] X. Liu, X. Liang, P. Wang, B. Huang, X. Qin, X. Zhang, Y. Dai, Appl. Catal. B: Environ. 203 (2017) 282–288.
- [51] K.J. Koski, Y. Cui, ACS nano 7 (2013) 3739–3743.
- [52] S. Liang, L. Wen, S. Lin, J. Bi, P. Feng, X. Fu, L. Wu, Angew. Chem. Int. Ed. 53 (2014) 2951–2955.
- [53] J. Xiong, Y. Liu, C. Cao, L. Shen, W. Wu, S. Liang, R. Liang, L. Wu, J. Mater. Chem. A 3 (2015) 6935–6942.
- [54] S. Gao, Y. Lin, X. Jiao, Y. Sun, Q. Luo, W. Zhang, D. Li, J. Yang, Y. Xie, Nature 529 (2016) 68–71.
- [55] J. Di, J. Xia, H. Li, Z. Liu, Nano Energy 35 (2017) 79–91.
- [56] M. Chhowalla, Z. Liu, H. Zhang, Chem. Soc. Rev. 44 (2015) 2584–2586.
- [57] D. Deng, K.S. Novoselov, Q. Fu, N. Zheng, Z. Tian, X. Bao, Nature nanotechnol. 11 (2016) 218–230.
- [58] B. Mahler, V. Hoepfner, K. Liao, G.A. Ozin, J. Am. Chem. Soc. 136 (2014) 14121–14127.
- [59] S. Liu, Z.R. Tang, Y. Sun, J.C. Colmenares, Y.J. Xu, Chem. Soc. Rev. 44 (2015) 5053–5075.
- [60] Q. Lu, Y. Yu, Q. Ma, B. Chen, H. Zhang, Adv. Mater. 28 (2016) 1917–1933.
- [61] D. Voiry, J. Yang, M. Chhowalla, Adv. Mater. 28 (2016) 6197–6206.
- [62] J.L. Xie, C.X. Guo, C.M. Li, Energy Environ. Sci. 7 (2014) 2559.
- [63] Z. Han, G. Chen, C. Li, Y. Yu, Y. Zhou, J. Mater. Chem. A 3 (2015) 1696–1702.
- [64] B. Weng, S. Liu, N. Zhang, Z.-R. Tang, Y.-J. Xu, J. Catal. 309 (2014) 146–155.
- [65] F.-X. Xiao, J. Miao, B. Liu, J. Am. Chem. Soc. 136 (2014) 1559–1569.
- [66] J. Low, S. Cao, J. Yu, S. Wageh, Chem. Commun. 50 (2014) 10768–10777.
- [67] W. Zhou, Z. Yin, Y. Du, X. Huang, Z. Zeng, Z. Fan, H. Liu, J. Wang, H. Zhang, Small 9 (2013) 140–147.
- [68] Q. Liu, H. Lu, Z. Shi, F. Wu, J. Guo, K. Deng, L. Li, ACS Appl. Mater. Inter. 6 (2014) 17200–17207.
- [69] B. Xu, P. He, H. Liu, P. Wang, G. Zhou, X. Wang, Angew. Chem. Int. Ed. 53 (2014) 2339–2343.
- [70] B. Han, S. Liu, Y.-J. Xu, Z.-R. Tang, RSC Adv. 5 (2015) 16476–16483.
- [71] Q. Liu, F. Cao, F. Wu, S. Chen, J. Xiong, L. Li, ACS Appl. Mater. Inter. 8 (2016) 26235–26243.
- [72] S. Shen, A. Ma, Z. Tang, Z. Han, M. Wang, Z. Wang, L. Zhi, J. Yang, ChemCatChem 7 (2015), 535–535.
- [73] W. Feng, Z. Fang, B. Wang, L. Zhang, Y. Zhang, Y. Yang, M. Huang, S. Weng, P. Liu, J. Mater. Chem. A 5 (2017) 1387–1393.
- [74] J. Yu, J. Zhang, M. Jaroniec, Green Chem. 12 (2010) 1611.
- [75] Q. Nie, Q. Yuan, Q. Wang, Z. Xu, J. Mater. Sci. 39 (2004) 5611–5612.

- [76] J. Zhao, J. Yin, M. Yang, J. Alloy. Compd. 579 (2013) 45–49.
- [77] A. Hernández-Gordillo, F. Tzompantzi, R. Gómez, Catal. Commun. 19 (2012) 51–55.
- [78] J. Jang, C. Yu, S. Choi, S. Ji, E. Kim, J. Lee, J. Catal. 254 (2008) 144–155.
- [79] J. Liu, Z. Guo, F. Meng, T. Luo, M. Li, J. Liu, Nanotechnology 20 (2009) 125501.
- [80] A. Brayek, S. Chaguetmi, M. Ghoul, I. Ben Assaker, A. Souissi, L. Mouton, P. Beaunier, S. Nowak, F. Mammeri, R. Chtourou, S. Ammar, RSC Adv. 6 (2016) 30919–30927.
- [81] X. Zhang, Z. Zhao, W. Zhang, G. Zhang, D. Qu, X. Miao, S. Sun, Z. Sun, Small 12 (2016) 793–801.
- [82] G. Wang, B. Huang, Z. Li, Z. Lou, Z. Wang, Y. Dai, M.H. Whangbo, Sci. Rep. 5 (2015) 8544.
- [83] Y.-C. Chen, H.-S. Chen, S.-R. Chung, J.-K. Chang, K.-W. Wang, J. Mater. Chem. C 3 (2015) 5881–5884.